The method is of doubtful use for structure determination or quantitative analysis. The wide range of wavelengths, continually varying absorption and profile widths, and other factors create a major difficulty in deriving accurate values of the relative intensities.

Conventional energy-dispersive diffraction methods using white X-rays and a solid-state detector are described in Chapter 2.5 and Section 5.2.7.

## 2.3.3. Specimen factors, angle, intensity, and profile-shape measurement

The basic experimental procedure in powder diffraction is the measurement of intensity as a function of scattering angle. The profile shapes and $2\theta$ angles are derived from the observed intensities and hence the counting statistical accuracy has an important role. There is a wide range of precision requirements depending on the application and many factors are involved: instrument factors, counting statistics, profile shape, and particle-size statistics of the specimen. *The quality of the specimen preparation is often the most important factor in determining the precision of powder diffraction data.*

D. K. Smith and colleagues (see, for example, Borg & Smith, 1969; see also Yvon, Jeitschko & Parthé, 1977) developed a method for calculating theoretical powder patterns from well determined single-crystal structures and have made available a Fortran program (Smith, Nichols & Zolensky, 1983). This has important uses in powder diffraction studies because it provides reference data with correct $I$'s and $d$'s, free of sample defects, preferred orientation, statistical errors, and other factors. The data can be displayed as recorded patterns by using plot parameters corresponding to the experimental conditions (Subsection 2.3.3.9). Calculated patterns have been used in a large variety of studies such as identification standards, computing intermediate members of an isomorphous series, testing structure models, ordered and disordered structures, and others. Many experiments can be performed with simulated patterns to plan and guide research. The method must be used with some care because it is based on the small single crystal used in the crystal-structure determination and the large powder samples of minerals and ceramics, for example, may have a different composition. Errors in the structure analysis are magnified because the powder intensities are based on the squares of the structure factors.

The Lorentz and polarization factors for diffractometry geometry have been discussed by Ladell (1961) and Pike & Ladell (1961).

Smith & Snyder (1979) have developed a criterion for rating the quality of powder patterns; see also de Wolff (1968*a*).

### 2.3.3.1. *Specimen factors*

Ideally, the specimen should contain a large number of small equal-sized randomly oriented particles. The surface must be flat and smooth to avoid microabsorption effects, *i.e.* particle interferences which reduce the intensities of the incident and reflected beams and can lead to significant errors (Cline & Snyder, 1983). The specimen should be homogeneous, particularly if it is a mixture or if a standard has been added. Low packing density and specimen-surface displacement (§2.3.1.1.6) may cause significant errors. It is recommended that the powder and the prepared specimen be examined with a low-power binocular optical microscope. Smith & Barrett (1979), Jenkins, Fawcett, Smith, Visser, Morris & Frevel (1986), and Bish & Reynolds (1989) have surveyed methods of specimen preparation and they include bibliographies on special handling problems. Powder diffraction standards for angle and intensity calibration are described in Section 5.2.9.

#### 2.3.3.1.1. *Preferred orientation*

Preferred orientation changes the relative intensities from those obtained with a randomly oriented powder sample. It occurs in materials that have good cleavage or a morphology that is platy, acicular or any special shape in which the particles tend to orient themselves in specimen preparation. The micas and clay minerals are examples of materials that exhibit very strong preferred orientation. When they are prepared as reflection specimens, the basal reflections dominate the pattern. It is common in prepared thin films where preferred orientation occurs frequently or may be purposely induced to enhance certain optical, electrical, or magnetic properties for electronic devices. By comparison of the relative intensities with the random powder pattern, the degree of preferred orientation can be observed.

Powder reflections take place from crystallites oriented in different ways in the instrument geometries as shown in Fig. 2.3.1.2. In reflection specimen geometry with $\theta$–$2\theta$ scanning, reflections can occur only from lattice planes parallel to the surface and in the transmission mode they must be normal to the surface. In the Seemann–Bohlin and fixed specimen with $2\theta$ scanning methods, the orientation varies from parallel to about 45° inclination to the surface. The effect of preferred orientation can be seen in diffraction patterns obtained by using the same specimen in the different geometries.

The effect is illustrated in Fig. 2.3.3.1 for *m*-chlorobenzoic acid, $C_7H_5ClO_2$, with reflection and transmission patterns and the pattern calculated from the crystal structure. The degree of preferred orientation is shown by comparing the peak intensities of four reflections in the three patterns:

| (*hkl*) | (120) | (200) | (040) | (121) |
|---|---|---|---|---|
| Reflection | 9.8 | 0.6 | 1.6 | 2.5 |
| Transmission | 5.2 | 0.5 | 0.7 | 9.3 |
| Calculated | 3.0 | 6.6 | 4.0 | 9.1. |

Care is required to make certain the differences are not caused by a few fortuitously oriented large particles.

Various methods have been used to minimize preferred orientation in the specimen preparation (Calvert, Sirianni, Gainsford & Hubbard, 1983; Smith & Barrett, 1979; Jenkins *et al.*, 1986; Bish & Reynolds, 1989). These include using small particles, loading the powder from the back or side of the specimen holder, and cutting shallow grooves to roughen the surface. The powder has also been sifted directly on the surface of a microscope slide or single-crystal plate that has been wetted with the binder or petroleum jelly. Another method is to mix the powder with an inert amorphous powder such as Lindemann glass or rice starch, or add gum arabic, which after setting can be reground to obtain irregular particles. Any additive reduces the intensity and the peak-to-background ratio of the pattern. A promising method that requires a considerable amount of powder is to mix it with a binder and to use spray drying to encapsulate the particles into small spheres which are then used to prepare the specimen (Smith, Snyder & Brownell, 1979).

Preferred orientation would not cause a serious problem in routine identification providing the reference standard had a similar preferred orientation and both patterns were obtained with the same diffractometer geometry. However, when accurate values of the relative intensities are required, as in crystal-

structure refinement and quantitative analysis, it may be the major factor limiting the precision.

In practice, it is very difficult to prepare specimens that have a completely random orientation. Even materials that do not have good cleavage or special morphological forms, such as quartz and silicon, show small deviations from a completely random orientation. These show up as errors in the structure refinement and a correction factor is required.

An empirical correction factor determined by the acute angle $\varphi$ between the preferred-orientation plane and the diffracting plane ($hkl$)

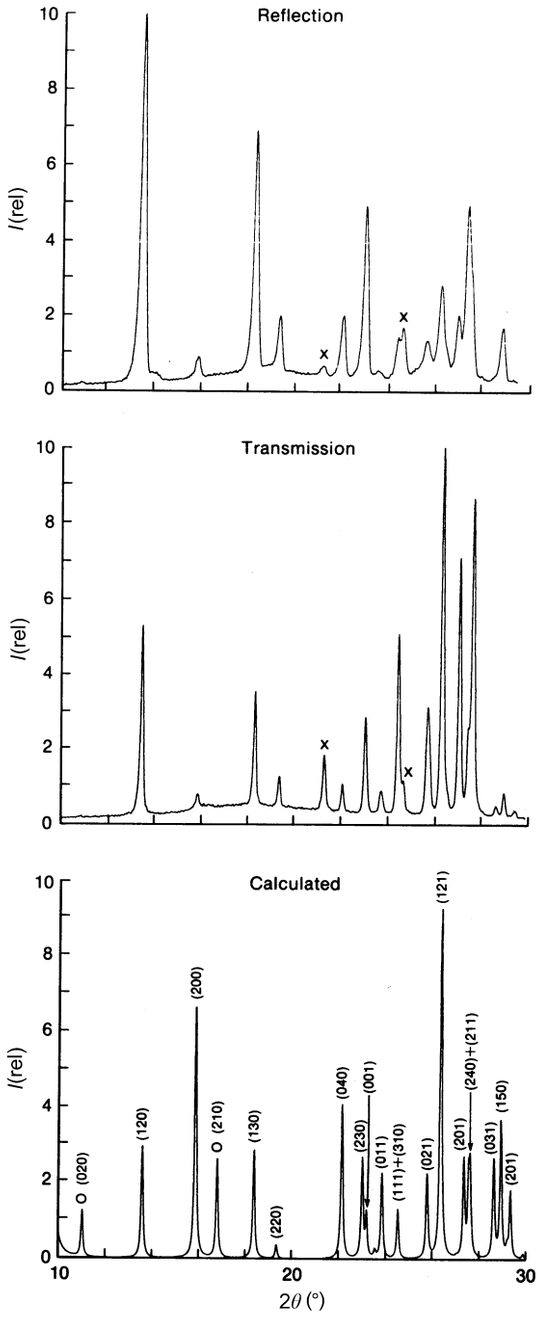


Fig. 2.3.3.1. Differences in relative intensities due to preferred orientation as seen in synchrotron X-ray patterns of *m*-chlorobenzoic acid obtained with a specimen in reflection and transmission compared with calculated pattern. Peaks marked × are impurities, *O* absent in experimental patterns.

Table 2.3.3.1. *Preferred-orientation data for silicon*

| $h\ k\ l$ | $R$(Bragg) (%) | GP |
|---|---|---|
| 1 1 1 | 1.86 | −0.11 |
| 2 2 0 | 2.02 | −0.11 |
| 3 1 1 | 2.01 | 0.17 |
| 4 0 0* | 0.86 | −0.15 |
| 3 3 1 | 1.73 | −0.19 |
| 4 2 2 | 2.43 | 0.04 |
| 5 1 1 | 1.36 | 0.19 |
| 5 3 1 | 2.44 | −0.08 |
| 4 4 2 | 1.69 | −0.19 |
| 6 2 0 | 1.25 | 0.29 |
| 5 3 3 | 2.40 | −0.04 |

* Selected preferred orientation plane.

Table 2.3.3.2. *R(Bragg) values obtained with different preferred-orientation formulae*

| | $R$(Bragg) | | |
|---|---|---|---|
| | Si | $SiO_2$ | $Mg_2GeO_4$ |
| No corrections | 3.50 | 2.57 | 12.5 |
| Gaussian | 1.65 | 1.60 | 5.71 |
| Exponential | 0.75 | 1.83 | 5.30 |
| March/Dollase | 0.75 | 1.64 | 4.87 |
| Preferred-orientation plane | 100 | 211 | 100 |

$$I(\text{corr.}) = I(hkl)P(hkl)\varphi \qquad (2.3.3.1)$$

can be used (Will *et al.*, 1988). Three functions have been used to represent $P(hkl)\varphi$ and the term GP is the variable refined:

$$P(hkl)\varphi = \exp(-\text{GP}\varphi^2) \qquad (2.3.3.2)$$

(Rietveld, 1969) for transmission specimens;

$$P(hkl)\varphi = \exp[\text{GP}(\pi/2 - \varphi^2)] \qquad (2.3.3.3)$$

for reflection specimens; and

$$P(hkl)\varphi = (\text{GP}^2 \cos^2\varphi + \sin^2\varphi/\text{GP})^{-3/2} \qquad (2.3.3.4)$$

(Dollase, 1986).

These functions are quite similar for small amounts of non-randomness. The preferred-orientation plane is selected by trial and error. For example, a modified fast routine of the powder least-squares refinement program with only seven cycles of refinement on each plane for the first dozen allowed Miller indices can be used to find the plane that gives the lowest $R$(Bragg) value as shown in Table 2.3.3.1. All three functions improve the $R$(Bragg) value as shown in Table 2.3.3.2 but the evidence is not conclusive as to which is the best. More research is required in this area. Several specimens made of the same material may show different preferred-orientation planes, and in some cases the preferred-orientation plane never occurred in the crystal morphology. A more complicated method examines the polar-axis density distribution using a cubic harmonic expansion to describe the crystallite orientation of a rotating sample (Järvinen, Merisalo, Pesonen & Inkinen, 1970; Ahtee, Nurmela, Suortti & Järvinen, 1989; Järvinen, 1993).

2.3.3.1.2. *Crystallite-size effects*

In addition to profile broadening, which begins to appear when the crystallite sizes are $< 1$–$2\,\mu m$, the sizes have a strong effect on the absolute and relative intensities (de Wolff, Taylor & Parrish, 1959; Parrish & Huang, 1983). The particle sizes have to be less than about $5\,\mu m$ to achieve 1% reproducible relative intensities from a stationary specimen in conventional diffractometer geometry (Klug & Alexander, 1974). The statistical errors arising from the number of particles irradiated can be greatly reduced by using smaller particles and rotating the specimen around the diffraction vector. This brings many more particles into reflecting orientations.

The particle-size effect is illustrated in Fig. 2.3.3.2 for specimens of NIST silicon standard powder 640 sifted to different size fractions. The powders were packed in a 1 mm deep cavity in a 25.4 mm diameter Al holder using 5% collodion/amyl acetate binder. They were rotated by a synchronous motor (a stepper motor can also be used) around the axis normal to the centre of the specimen surface with the detector arm fixed at the peak position and the intensity recorded with a strip-chart. Rapid rotation, $\sim 60\,r\,min^{-1}$, gives the average peak intensity for all azimuths of the specimen and the small variations result only from the counting statistics. Scaling the intensities to (111) = 100% for the 5–10 μm fraction, the 10–20 μm fraction is 94%, 20–30 μm 88% and > 30 μm 59%. The decrease is probably due to lower particle-packing density and increasing interparticle microabsorption. The > 5 μm fraction = 95% may be due to the larger ratio of oxide coating around the particles to the mass of the particles.

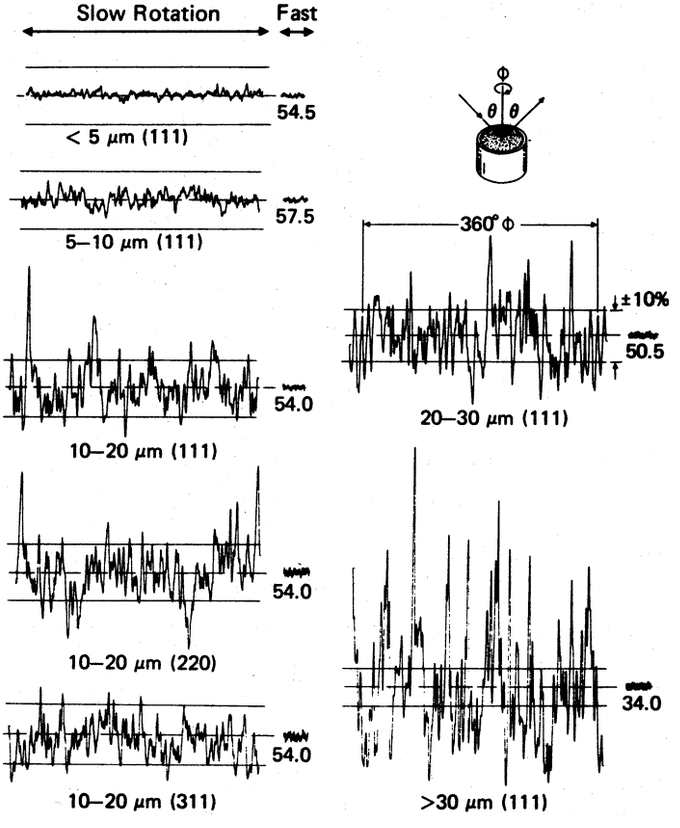


Fig. 2.3.3.2. Effect of specimen rotation and particle size on Si powder intensity using a conventional diffractometer (Fig. 2.3.1.3) and Cu $K\alpha$. Numbers below fast rotation are the average intensities.

Slow rotation, $\sim 1/7\,r\,min^{-1}$, shows the variation of the peak intensity with azimuth angle $\varphi$. The pattern repeats after 360° rotation and the magnitude of the fluctations increases with increasing particle sizes and resolution. There is no correlation between the fluctations of different reflections, as can be seen by comparing the 111, 220 and 311 reflections of the 10–20 μm specimen (lower left side) for which the incident-beam intensity was adjusted to give the same average amplitude. The horizontal lines are ±10% of the average. This shows the magnitude of errors that could occur using stationary specimens. Similar particle-size effects were found using the integrated intensities derived from profile fitting. The above discussion and Fig. 2.3.3.2 refer to a continuous scan. If the step-scan mode is used to collect data, it is clearly not necessary to rotate the specimen through more than one revolution at each step.

The rotating specimen also averages the in-plane preferred orientation but has virtually no effect on the planes oriented parallel to the specimen surface. The slow rotation method is useful in testing the grinding and sifting stages in specimen preparation. When calibrated with known size fractions, it can be used as a rough qualitative measure of the particle sizes.

2.3.3.2. *Problems arising from the Kα doublet*

A common source of error arises from the $K\alpha$ doublet which produces a pair of peaks for each reflection. The separation of the Cu $K\alpha_1$, $K\alpha_2$ peaks increases from 0.05° at 20°2θ to 1.08° at 150°2θ. The overlapping is also dependent on the instrument resolution and may cause errors in the peak angles and intensities when strip-chart recording or peak-search methods (described below) are used. The $K\alpha_1$ wavelength is generally used to calculate all the $d$'s even when the low-angle peaks are unresolved. In the region where the doublet is only slightly resolved, the apparent $K\alpha_1$ peak angle is shifted to higher angles because of the overlapping $K\alpha_2$ tail and similarly the peak intensities will be in error. The relative peak intensities of a reflection with superposed doublet compared to a resolved doublet could have an error as large as 50%. Relative peak intensities are used in the ICDD standards file and cause no problem because the unknowns are measured in the same way. The integrated intensity avoids this difficulty but is impractical to use in routine identification.

Rachinger (1948) described a simple graphical procedure for removing $K\alpha_2$ peaks. The method causes errors because it makes the incorrect assumption that $K\alpha_2$ is the exact half-scale version of $K\alpha_1$. Ladell, Zagofsky & Pearlman (1975) developed an exact algorithm using the actual mathematical shapes observed with

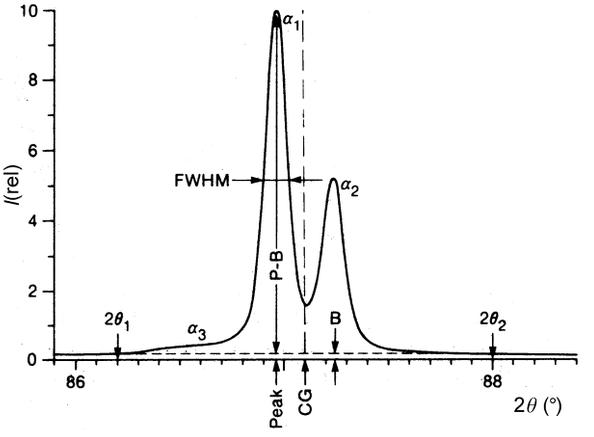


Fig. 2.3.3.3. Various measures of profile.

the user's diffractometer but, with line-profile-fitting programs now available, the $K\alpha_2$ component can be modelled precisely along with the $K\alpha_1$.

It is possible to isolate the $K\alpha_1$ line when using a high-quality incident-beam focusing monochromator as described in Subsection 2.3.1.2, Fig. 2.3.1.12(*b*), but there may be a loss of intensity. The source size must be narrow and the focal length long enough to separate the components.

### 2.3.3.3. *Use of peak or centroid for angle definition*

The most obvious and commonly used measure of the reflection angle of a profile is the position of maximum intensities (Fig. 2.3.3.3). The midpoints of chords at various heights have often been used but their values vary with the profile asymmetry. Another method is to connect the midpoints of chords near the top of the profile and extrapolate to the peak. The computer methods using derivatives are the most accurate and fastest as described in Subsection 2.3.3.7.

A more fundamental measure that uses the entire intensity distribution is the centre of gravity (or centroid) defined as

$$\langle 2\theta\rangle = \int 2\theta I(2\theta)\,\mathrm{d}(2\theta) \Big/ \int I(2\theta)\,\mathrm{d}(2\theta). \qquad (2.3.3.5)$$

The variance (mean-square deviation of the mean) is defined as

$$W_{2\theta} = \langle(2\theta - \langle 2\theta\rangle)^2\rangle = \int(2\theta - \langle 2\theta\rangle)^2 I(2\theta)\,\mathrm{d}(2\theta) \Big/ \int I(2\theta)\,\mathrm{d}(2\theta). \qquad (2.3.3.6)$$

The use of the centroid and variance has two important advantages: (1) most of the aberrations (§2.3.1.1.6) were derived in terms of the centroid and variance; and (2) they are additive, making it easy to determine the composite effect of a number of aberrations. Mathematically, the integration extends from $-\infty$ to $+\infty$ but the aberrations have a finite range. However, the practical use of these measures causes some difficulty. If the profile shapes are Lorentzian, the tails decay slowly. A very wide range would be required to reach points where the signal could no longer be separated from the background and the profiles must be truncated for the calculation. Truncation limits that have been used are 90% ordinate heights of $K\alpha_1$ (Ladell, Parrish & Taylor, 1959), and equal $2\theta$ or $\lambda$ limits from the centroid (Taylor, Mack & Parrish, 1964; Langford, 1982). The limits such as $2\theta_1$ and $2\theta_2$ in Fig. 2.3.3.3 must be carefully chosen to avoid errors and this involves the correct determination of the background level. It is not practical to use centroids for overlapping peak clusters unless the profile fitting can accurately resolve the individuals with their correct positions and intensities. Their use has, therefore, been confined to simple patterns with small unit cells in which the profiles were well separated.

The difference between the angle derived from the peak and the centroid depends on the asymmetry of the profile, which in turn varies with the $K\alpha$-doublet separation and the aberration broadening. Tournarie (1958) found that the centre of a horizontal chord at 60.6% of the $K\alpha_1$ peak height corresponds well to the centroid of that line in fairly well resolved doublets. The number, of course, depends on the profile shape. There is also the basic problem that most of the X-ray wavelengths were probably determined from the spectral peaks and, if the centroids are measured for the powder pattern, the Bragg equation becomes nonlinear in the sense that the 1:1 correspondence between $\lambda$ and $\sin\theta$ is lost.

### 2.3.3.4. *Rate-meter/strip-chart recording*

Formerly, the most common method of obtaining diffractometer data was by using a rate-meter and strip-chart recorder with the paper moving synchronously with the constant angular velocity of the scan. This simple analogue method is still used and a large fraction of the JCPDS (ICDD) file prior to about 1982 was obtained in this way.

The method has several limitations: the data are not in the digital form required for computers, and are distorted; manual measurement of the chart takes a long time and has low accuracy. The output of the strip chart lags behind the input by an amount determined by the product of the scanning speed and the time constant of the rate-meter, including the speed of the recorder pen. The peak height is decreased and shifted in the direction of the scan causing asymmetric broadening with loss of resolution. The profile shape, $K\alpha$-doublet separation, and scan direction also contribute to distortion. When the product of the scan speed and time constant have the same value, the profile shapes are the same even though the total count is determined by the scan speed, Figs. 2.3.3.4(*a*) and (*b*). If the product is large, the distortion is severe (*c*), and very weak peaks may be lost.

### 2.3.3.5. *Computer-controlled automation*

Most diffractomers are now sold with computer automation. Older instruments can be easily upgraded by adding a stepping motor to the gear-drive shaft. A large variety of computers and programs is available, and it is not easy to make the best selection. Continuing improvements in computer technology have been made to handle expanded programs with increased speed and storage capabilities. The collected data are displayed on a VDU screen and/or computer printer and stored on hard disk or diskette for later use and analysis. Microprocessors are often used to select the X-ray-generator operating conditions, shutter control, specimen change, and similar tasks that were formerly performed manually. Aside from the elimination of much of the manual labour, automation provides far better control of the data-collection and data-reduction procedures. However, computers do not preclude the necessity of precise alignment and calibration. Smith (1989) has written a detailed description of computer analysis for phase identification and also includes related programs and their sources.

Personal computers are widely used for powder-diffraction automation and a typical arrangement is shown in Fig. 2.3.3.5(*a*). The automation may provide for step scanning,

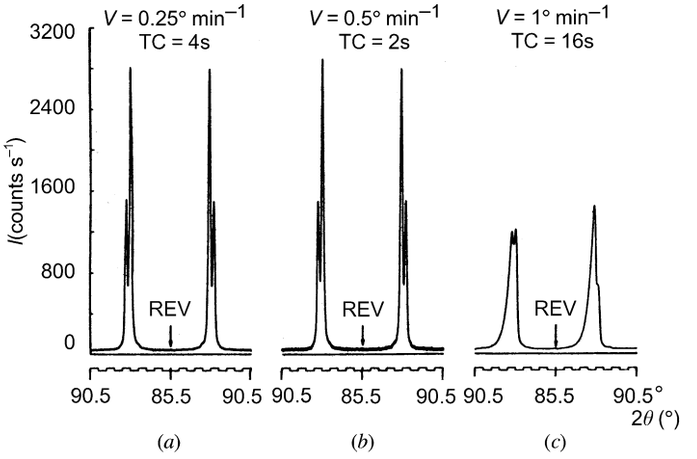


Fig. 2.3.3.4. Rate-meter strip-chart recordings. REV: scan direction reversed. Scan speed and time constant shown at top.

continuous scanning with read-out on the fly, or slewing to selected angles to read particular points. Step scanning is the method most frequently used. It is essential that absolute registration and step tracking be reliably maintained for all experimental conditions.

The step size or angular increment $\Delta 2\theta$ and count time $t$ at each step, and the beginning and ending angles are selectable. For a given total time available for the experiment, it usually makes no difference in the counting statistical accuracy if a combination of small or large $\Delta 2\theta$ and $t$ (within reasonable limits) is used. A minimal number of steps of the order of $\Delta 2\theta \simeq 0.1$ to 0.2 FWHM is required for profile fitting isolated peaks. It is clear that the greater the number of steps, the better the definition of the profile shape. The step size becomes important when using profile fitting to resolve patterns containing overlapped reflections and to detect closely spaced overlaps from the width and small changes in slopes of the profiles. A preliminary fast run to determine the nature of the pattern may be made to select the best run conditions for the final pattern. Will *et al.* (1988) recorded a quartz pattern with 1.28 Å synchrotron X-rays and 0.01° steps to test the step-size role. The profile fitting was done using all points and repeated with the omission of every second, third, and fourth point corresponding to $\Delta 2\theta = 0.02$, 0.03 and 0.04°. The $R$(Bragg) values were virtually the same (except for 0.04° where it increased), indicating the experimental time could have been reduced by a factor of three with little loss of precision; see also Hill & Madsen (1984). Patterns with more overlapping would require smaller steps. Ideally, the steps could be larger in the background but this also requires a prior knowledge of the pattern and special programming.

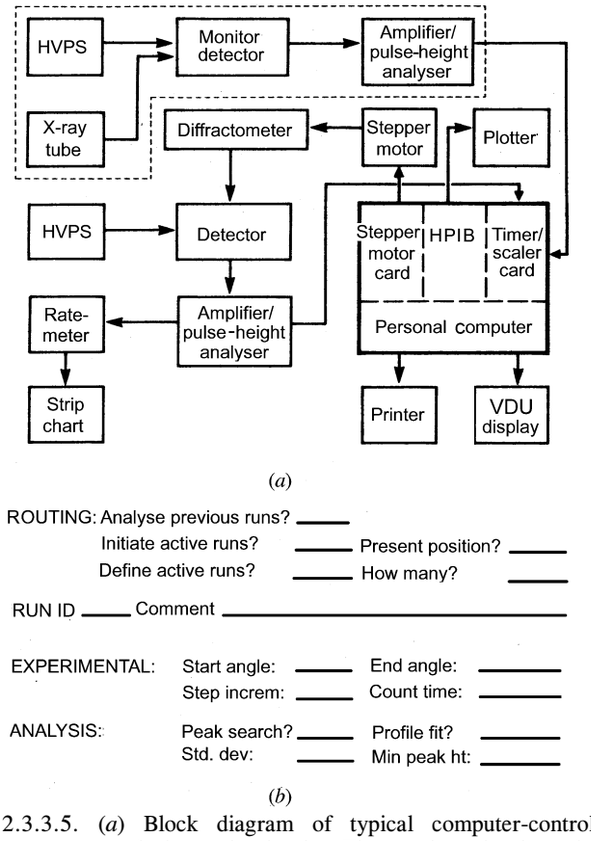


Fig. 2.3.3.5. (*a*) Block diagram of typical computer-controlled diffractometer and electronic circuits. The monitor circuit enclosed by the dashed line is optional. HPIB is the interface bus. (*b*) A full-screen menu with some typical entries.

A typical VDU screen menu for diffractometer-operation control is shown in Fig. 2.3.3.5(*b*). A number of runs can be defined with the same or different experimental parameters to run consecutively. The run log number, date, and time are usually automatically entered and together with the comment and parameters are carried forward and recorded on the print-outs and graphics to make certain the runs are completely identified. The menu is designed to prompt the operator to enter all the required information before a run can be started. Error messages appear if omissions or entry mistakes are made. There are, of course, many variations to the one shown.

### 2.3.3.6. *Counting statistics*

X-ray quanta arrive at the detector at random and varying rates and hence the rules of statistics govern the accuracy of the intensity measurements. The general problems in achieving maximum accuracy in minimum time and in assessing the accuracy are described in books on mathematical statistics. Chapter 7.5 reviews the pertinent theory; see also Wilson (1980). In this section, only the fixed-time method is described because the fixed-count method takes too long for most practical applications.

Let $\bar{N}$ be the average of $N$, the number of counts in a given time $t$, over a very large number of determinations. The spread is given by a Poisson probability distribution (if $\bar{N}$ is large) with standard deviation

$$\sigma = \bar{N}^{1/2}. \tag{2.3.3.7}$$

Any individual determination of $N$ or the corresponding counting rate $n$ $(= N/t)$ will be subject to a proportionate error $\varepsilon$ which is also a function of the confidence level, *i.e.* the probability that the result deviates less than a certain percentage from the true value. If $Q$ is the constant determined by the confidence level, then

$$\varepsilon = Q/N^{1/2}, \tag{2.3.3.8}$$

where $Q = 0.67$ for the probable relative error $\varepsilon_{50}$ (50% confidence level) and $Q = 1.64$ and 2.58 for the 90 and 99% confidence levels ($\varepsilon_{90}$, $\varepsilon_{99}$), respectively. For a 1% error, $N = 4500$, 27 000, 67 000 for $\varepsilon_{50}$, $\varepsilon_{90}$, $\varepsilon_{99}$, respectively. Fig. 2.3.3.6 shows various percentage errors as a function of $N$ for several confidence levels.

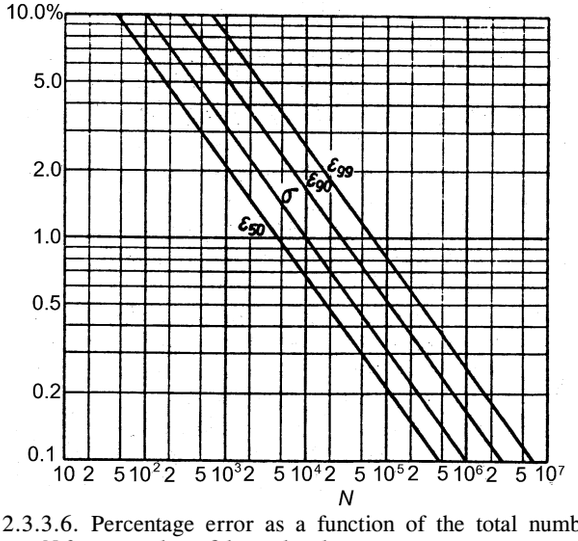


Fig. 2.3.3.6. Percentage error as a function of the total number of counts $N$ for several confidence levels.

In practice, there is usually a background count $N_B$. The net peak count $N_{P+B} - N_B = N_{P-B}$ is dependent on the $P/B$ radio as well as on $N_{P+B}$ and $N_B$ separately. The relative error $\varepsilon_D$ of the net peak count is

$$\varepsilon_D = \frac{[(N_{P+B}\varepsilon_{P+B})^2 + (N_N\varepsilon_B)^2]^{1/2}}{N_{P-B}}, \qquad (2.3.3.9)$$

which shows that $\varepsilon_D$ is similarly influenced by both absolute errors $N_{P+B}\varepsilon_{P+B}$ and $N_B\varepsilon_B$. The absolute standard deviation of the net peak height is

$$\sigma_{P-B} = (\sigma_{P+B}^2 + \sigma_B^2)^{1/2} \qquad (2.3.3.10)$$

and expressed as the per cent standard deviation is

$$\sigma_{P-B} = \frac{(N_{P+B} + N_B)^{1/2}}{N_{P-B}} \times 100. \qquad (2.3.3.11)$$

The accuracy of the net peak measurement decreases rapidly as the peak-to-background ratio falls below 1. For example, with $N_B = 50$, the dependence of $\sigma_{P-B}$ on $P/B$ is

| $P/B$ | $\sigma_{P-B}$ (%) |
|---|---|
| 0.1 | 205 |
| 1 | 24.5 |
| 10 | 4.9 |
| 100 | 1.43. |

It is obviously desirable to minimize the background using the best possible experimental methods.

### 2.3.3.7. *Peak search*

The accurate location of the $2\theta$ angle corresponding to the peak of the profile has been discussed in many papers (see, for example, Wilson, 1965). Computers are now widely used for data reduction, thereby greatly decreasing the labour, improving the accuracy, and making possible the use of specially designed algorithms. It is not possible to present a description of the large number of private and commercial programs. The peak-search and profile-fitting methods described below have been successfully used for a number of years and are representative of the results that can now be obtained. They have greatly improved the results in phase identification, integrated intensity measurement, and analyses requiring precise profile-shape determination. It is likely that even better programs and methods will be developed in this rapidly changing field.

There are two levels of the types of data reduction that may be done. The easiest and most frequently used method is usually called 'peak search'. It computes the $2\theta$ angles and intensities of the peaks. The results have good precision for isolated peaks but give the values of the composite overlapping reflections as they appear, for example, on a strip-chart recording. The calculation is virtually instantaneous and is often all that is needed for phase identification, lattice-parameter determination, and similar analyses. The second, profile fitting, described below, is a more advanced procedure that can resolve overlapping peaks into individual reflections and determines the profile shape, width, peak and integrated intensities, and reflection angle of each resolved peak. This method requires a prior knowledge of the profile-fitting function. It is used to determine the integrated intensities for analyses requiring higher precision such as crystal-structure refinement and quantitative analysis, and profile-shape parameters for small crystallite size, microstrain and similar studies.

To measure weak peaks, the counting statistical accuracy must be sufficient to delineate the peak from the background. When the intensity and peak-to-background ratio are low, the computing time is much increased. Since powder patterns often contain a number of weak peaks that may not be required for the analysis, computer programs often permit the user to select a minimum peak height (MPH) and a standard deviation (SD) that the peak must exceed to be included in the data reduction. For example, MPH = 1 would reject peaks less than 1% of the highest peak in the recorded pattern, and SD = 4 requires the intensity to exceed the background adjacent to the peak by $4B^{1/2}$. The number of peaks rejected depends on the intensity and peak-to-background ratio as illustrated in Fig. 2.3.3.7, where the cut-off level was set at $\bar{B} + 4\bar{B}^{1/2}$ for two recordings of the same pattern with about a 40 times difference in intensities. All visible peaks are included in the high-intensity recording and several are rejected by the cut-off level selected in the lower-intensity pattern.

Before carrying out the computer calculations, it may be desirable to subtract unusual background such as is caused by a glass substrate in a thin-film pattern.

The following method was developed using computer-generated profiles having the same shapes as conventional diffractometer (Fig. 2.3.1.3) profiles and adding random counting statistical noise (Huang & Parrish, 1984; Huang, 1988). The best results were obtained using the first derivative ($dx/dy = 0$) of a least-squares-fitted cubic polynomial to locate the peaks, combined with the second derivative ($d^2y/dx^2 = \text{minimum}$) of a quadratic/cubic polynomial to resolve overlapped reflections (Fig. 2.3.3.8). Overlaps with a separate $\geq 0.5$ FWHM can be resolved and measured and the accuracy of the peak position is 0.001° for noise-free profiles. Real profiles with statistical noise have a precision of ±0.003 to 0.02° depending on the noise level. The Savitzky & Golay (1964) method (see also Ateiner, Termonia & Deltour, 1974; Edwards & Willson, 1974) was used for smoothing and differentiation of

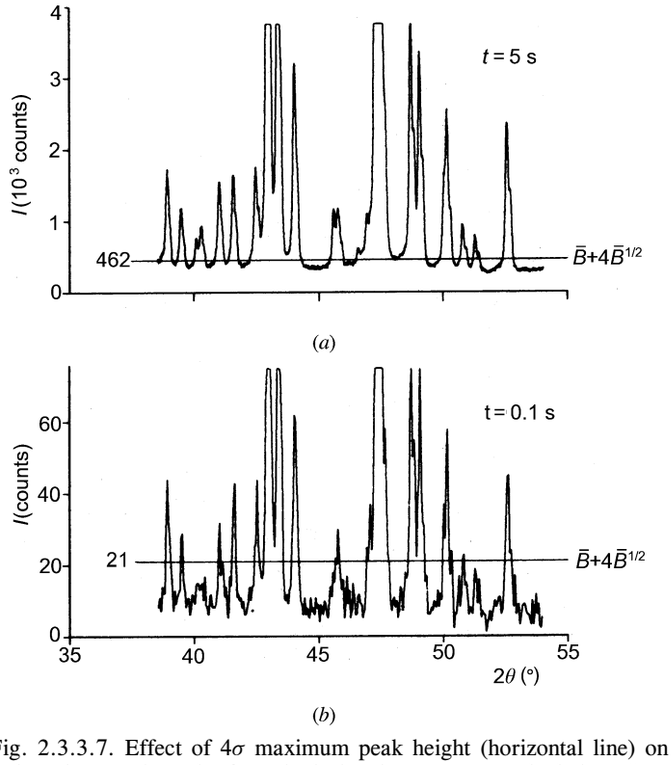


Fig. 2.3.3.7. Effect of $4\sigma$ maximum peak height (horizontal line) on dropping weak peaks from inclusion in computer calculation. Step scan with (*a*) $t = 5$ s and (*b*) $t = 0.1$ s. Five-compound mixture, Cu $K\alpha$.

the data by least squares in which the values of the derivatives can be calculated using a set of tabulated integers. The convolution range CR expressed as a multiple of the FWHM of the peak can be selected. A minimum of five points is required. For asymmetric peaks, such as occur at small $2\theta$'s, a CR $\simeq 0.5$ FWHM gives the best precision. The larger the CR the larger the intrinsic error but the smaller the random error, and the smaller the number of peaks identified in overlapping patterns. The larger CR also avoids false peaks in patterns with poor counting statistics. Fig. 2.3.3.8(*c*) shows the dependence of the accuracy of the peak determination on $P/\sigma$. The computer results list the $2\theta$'s, $d$'s, absolute and relative intensities (scaled to 100) of the identified peaks. The calculation is made with a selected wavelength such as $K\alpha_1$ and the possible $K\alpha_2$ peaks are flagged.

### 2.3.3.8. *Profile fitting*

Profile fitting has greatly advanced powder diffractometry by making it possible to calculate the intensities, peak positions, widths, and shapes of the reflections with a far greater precision than had been possible with manual measurements or visual inspection of the experimental data. The method has better resolution than the original data and the entire scattering distribution is used instead of only a few features such as the peak and width. Individual profiles and clusters of reflections can be fitted, or the entire pattern as in the Rietveld method (Chapter 8.6).

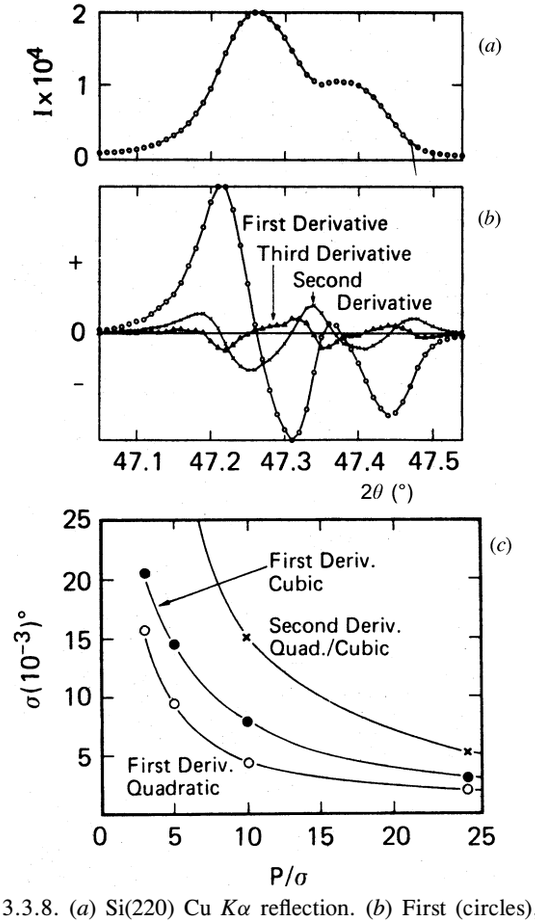


Fig. 2.3.3.8. (*a*) Si(220) Cu $K\alpha$ reflection. (*b*) First (circles), second (crosses), and third (triangles) derivatives of a seven-point polynomial of data in (*a*). (*c*) Average angular deviations as a function of $P/\sigma$ for various derivatives.

The procedure is based on the least-squares fitting of theoretical profile intensities to the digitized powder pattern. The profile intensity at the $i$th step is calculated by

$$Y(x_i)_{\rm calc} = B(x_i) + \sum_j I_j P(x_i - T_j)_j, \qquad (2.3.3.12)$$

where $B(x_i)$ is the background intensity, $I_j$ is the integrated intensity of the $j$th reflection, $T_j$ is the peak-maximum position, $P(x_i)_j$ is the profile function to represent the profile shape, and $\sum_j$ is taken over $j$, in which the $P(x)_j$ has a finite value at $x_i$. Unlike the Rietveld method, a structure model is not used. In the least-squares fitting, $I_j$ and $T_j$ are refined together with background and profile shape parameters in $P(x)_j$. Smoothing the experimental data is not required because it underestimates the estimated standard deviations for the least-squares parameters, which are based on the counting statistics.

The experimental profiles are a convolution of the X-ray line spectrum $\lambda$ and all the combined instrumental and geometrical

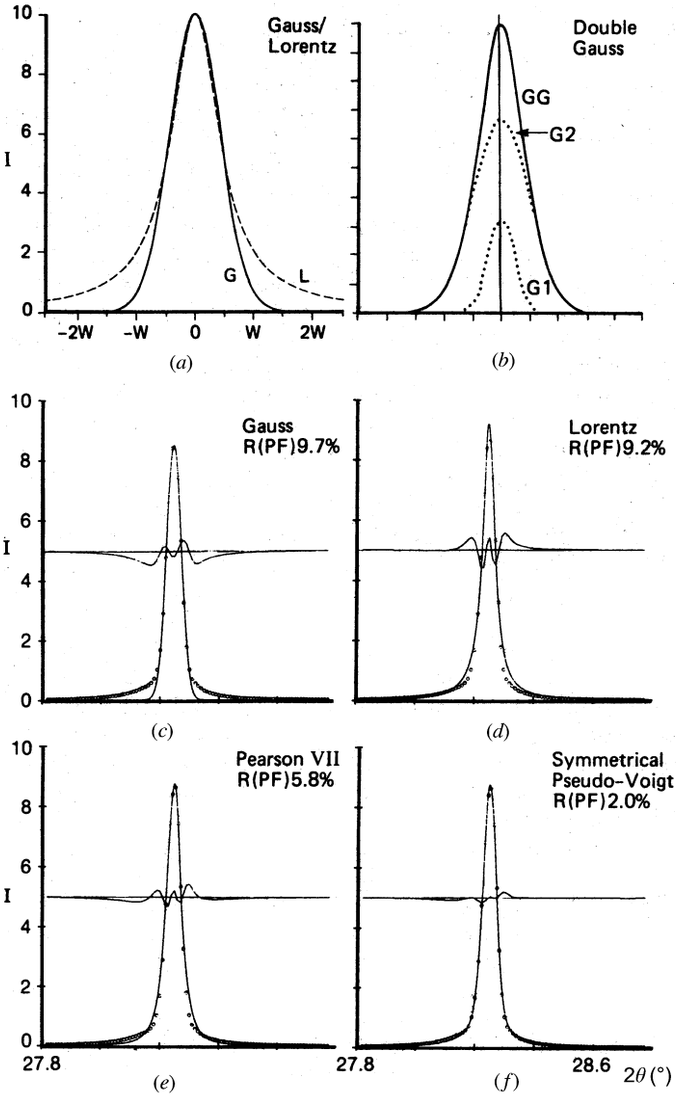


Fig. 2.3.3.9. (*a*) Computer-generated symmetrical Lorentzian profile $L$ and Gaussian $G$ with equal peak heights, $2\theta$ and FWHM. (*b*) Double Gaussian $GG$ shown as the sum of two Gaussians in which $I$ and FWHM of $G1$ are twice those of $G2$ and $2\theta$ is constant. (*c*)–(*f*) Profile fitting with different functions. Differences between experimental points and fitted profile shown at one-half height. Synchrotron radiation, Si(111).

aberrations $G$ with the true diffraction effects of the specimen $S$ (Parrish, Huang & Ayers, 1976), *i.e.*

$$\Omega(x) = (\lambda * G) * S + \text{background}. \qquad (2.3.3.13)$$

The profile shapes and resolution differ in the various diffractometer geometries and there is no universal profile-fitting function. In conventional X-ray tube focusing methods, the profiles are asymmetric and the shapes change continually across the scattering-angle range owing to the aberrations and the $K\alpha$ doublet. To avoid problems caused by the $K\alpha$ doublet, a few authors used the $K\beta$ line, but it has only about 1/7 the intensity. The profiles obtained with synchrotron radiation are symmetrical and narrower, and the widths increase with increasing $2\theta$. The different shapes and rates of decay of the tails make it necessary to find an analytical function that best fits the particular experimental profile. Langford (1987) and Young & Wiles (1982) have compiled and reviewed various profile-fitting functions and several are described below. Howard & Preston (1989) give details of the computations in their review of the method.

Early profile analyses used Gaussian or Lorentzian (Cauchy) curves. Fig. 2.3.3.9(*a*) shows that the most obvious difference is the rate of decay of the tails. X-ray synchrotron profiles lie between the two as shown in Figs. 2.3.3.9(*c*)–(*f*). The function must fit the tails as well as the main body and single-element functions are generally unsatisfactory. The Voigt function is a convolution of Lorenzian ($L$) and Gaussian ($G$) functions of different widths:

$$P(x)_V = \int L(x)G(x-u)\,\mathrm{d}u, \qquad (2.3.3.14)$$

where $x$ corresponds to $2\theta - T_j$ (Langford, 1978). It has been used for profile fitting and also to determine certain physical properties such as crystallite size and strain broadening from the constituent $L$ and $G$ profiles (see, for example, Langford, 1978; Suortti, Ahtee & Unonius, 1979; de Keijser, Langford, Mittemeijer & Vogels, 1982; Langford, Delhez, de Keijser & Mittemeijer, 1988). Evaluation of a symmetrical Voigt function involves the real part of the complex error function and an algorithm for calculating this has been given by Langford (1992).

The two most frequently used functions are at present the pseudo-Voigt (Wertheim, Butler, West & Buchanan, 1974) and the Pearson VII (Hall, Veeraraghavan, Rubin & Winchell, 1977). They cannot be easily deconvoluted analytically and have no direct physical interpretation but the equivalent Voigt parameters can be derived. Both can be split into symmetric and asymmetric portions to adjust better to the profile asymmetries and tails. The shapes can also be varied systematically by changing the $L/G$ ratio (de Keijser, Langford, Mittemeijer & Vogels, 1982).

The pseudo-Voigt function is similar to the Voigt except that an addition is used in place of the convolution. It is easier to use and Wertheim *et al.* (1974) found there was only a small difference in the intensities and widths obtained with this approximation. It is defined as

$$P(x)_{\mathrm{p-V}} = \eta L(x) + (1-\eta)G(x), \qquad (2.3.3.15)$$

where $\eta$ is the ratio of Lorentz to Gauss and they have the same widths. The refined $\eta$ and width of the full fitted profile can be related by a polynomial expansion (Hastings, Thomlinson & Cox, 1984; David, 1986; Cox, Toby & Eddy, 1988) to the widths of the $L$ and $G$ components of the original Voigt function. It is frequently used to fit synchrotron-radiation profiles. In the particular case shown in Figs. 2.3.3.9(*c*)–(*f*), the pseudo-Voigt has the best fit as shown by the difference curve at half-height and the lowest $R_p$[= $R$(PF)] value.

The Pearson VII function is defined as

$$P(x)_{\mathrm{PVII}} = a[1 + (x/b)^2]^{-m}, \qquad (2.3.3.16)$$

where $m$ is a refinable parameter based on the $G/L$ content (for $m = 1$, the curve is 100% Lorentzian and for $m = \infty$ it is 100% Gaussian), and $1/b = 2[2^{1/m} - 1]^{1/2}/W$, where $W$ is the FWHM.

The peak asymmetry can be incorporated into the profile function in several ways. One is to multiply (or add) the symmetrical profile function with an asymmetric function (Rietveld, 1969). Another is to dispose two or three functions asymmetrically (Parrish, Huang & Ayers, 1976). A third is to use a split-type function, consisting of two profile functions, each of which defines one-half the total peak, *i.e.* the low- or high-angle sides of the peak and each has different profile widths and shapes but the same height (Toraya, Yoshimura & Somiya, 1983; Howard & Snyder, 1983).

Some other functions that have been used include the double Gaussian [Fig. 2.3.3.9(*b*)] for low-resolution synchrotron data (Will, Masciocchi, Parrish & Hart, 1987), a Gaussian with shifted Lorentzian component to account for the asymmetry on the low-$2\theta$ side of the tail (Will, Masciocchi, Parrish & Lutz, 1990), profile modelling of single isolated peaks with a rational function, *e.g.* the ratio of two polynomials (Pyrros & Hubbard, 1983). In contrast to these analytical-type functions, some empirical functions have been developed. They are the 'learned' (experimental) peak-shape function (Hepp & Baerlocher, 1988) and the direct fitting of experimental data represented by Fourier series (Mortier & Constenoble, 1973).

The sum of Lorentzians has been used for X-ray tube focusing profiles (Parrish & Huang, 1980; Taupin, 1973). The instrument function ($\lambda * G$) is determined (see below) by a sum of Lorentzian curves, three each for $K\alpha_1$ and $K\alpha_2$ and one for the weak $K\alpha_3$ satellite. Three Lorentzians were used to match the asymmetry although a greater or lesser number could be used depending on the profile symmetry. Each curve has three parameters (intensity, half-width at half-height, and peak position) and the 21 parameters are adjusted by the computer program to give the best fit to the experimental data, which may contain 150 to 300 points. This is done only once for each particular instrument set-up. After ($\lambda * G$) is determined, the profile fitting is easy and fast because only the specimen contribution $S$ must be convoluted with ($\lambda * G$). If the specimen has no asymmetric broadening other than ($\lambda * G$), $S$ can be approximated by a single symmetrical Lorentzian for each reflection; a split Lorentzian can be used if there is asymmetric broadening.

A function can be tested using isolated profiles of a standard specimen such as silicon, tungsten, quartz, and others which have $< 10\,\mu$m particles and no specimen broadening (Fawcett *et al.*, 1988). It is necessary to do this test carefully and whenever the instrument parameters are changed.

The instrument function can be measured using isolated profiles of standard specimens as stated above. The measurements should be made with small $\Delta 2\theta \simeq 0.01^\circ$ steps and count times long enough to accumulate about 25 000 to 50 000 counts on the $K\alpha_1$ peaks for good counting statistics. By measuring a number of profiles separated by no more than about 5 to 10°, the instrument function can be established for the angular range of interest. A linear interpolation of the profile-fitting parameter between adjacent profiles gives a continuous function for use at any $2\theta$ in the range. The

intensities of the derived profile parameters are normalized and stored in the computer for later use. Note that any change in the X-ray spectrum or instrument geometry requires another set of measurements. The instrument function is also an important aid in computer graphics as described in Subsection 2.3.3.9.

The fitting of conventional diffractometer profiles was considerably improved by the use of a convolution function, in which the Pearson VII function is convoluted with the observed instrument function (Toraya *et al.*, 1983; Toraya, 1988). Enzo, Fagherrazzi, Benedetti & Polizzi (1988; Benedetti, Fagherazzi, Enzo & Battagliarin, 1988) used the convolution of a pseudo-Voigt function as the true data function and the convolution of exponential and pseudo-Voigt functions as the instrumental function for crystallite size and strain analysis. These functions have advantages in analysing the crystallite size and strain, although they require longer computation time for calculating the convolution.

Background intensity is usually included in the refinement. A first- or second-order polynomial is used to represent the background function $B(x)$ in equation (2.3.3.12) in a small $2\theta$ range, and the polynomial coefficients are adjusted during the least-squares refinement. In some cases, the background is subtracted from the pattern before the refinement by using the lowest intensities between the reflections. The background in the vicinity of high-intensity peaks and peak clusters is usually higher and should be avoided.

In the least-squares refinement, the following quantity is minimized:

$$\Delta = \sum_{i=1}^{N} w_i [Y(x_i)_{\rm obs} - Y(x_i)_{\rm calc}]^2, \qquad (2.3.3.17)$$

where $N$ is the number of observations, $w_i$ is the weight assigned to the $i$th observation, and $Y(x_i)_{\rm obs}$ is the observed profile intensity. A statistical weighting factor such as $w_i = \sigma_i^2$, where $\sigma_i^2 = 1/Y(x_i)_{\rm obs}$, is frequently used. The quality of the fitting procedure is generally expressed by $R$ factors such as $R_{wp}$, the weighted $R$ factor for profile intensity, which includes the entire scattering range and the background. The definitions of these factors are summarized by Young, Prince & Sparks (1982). The $R_p$ and $R_{wp}$ factors are given as

$$R_p(\%) = 100 \sum_{i=1}^{N} |Y(x_i)_{\rm obs} - Y(x_i)_{\rm calc}| \Big/ \sum_{i=1}^{N} Y(x_i)_{\rm obs}, \qquad (2.3.3.18)$$

$$R_{wp}(\%) = 100 \left\{ \frac{\sum_{i=1}^{N} w_i \left[ Y(x_i)_{\rm obs} - Y(x_i)_{\rm calc} \right]^2}{\sum_{i=1}^{N} w_i Y(x_i)_{\rm obs}^2} \right\}^{1/2}. \qquad (2.3.3.19)$$

If the selected function is inappropriate, it will show up on the difference curve (experimental – calculated; see Fig. 2.3.3.9), and high $R_p$ and $R_{wp}$ factors.

A whole-powder-pattern fitting technique without using the structural model was proposed for analysing neutron powder data (Pawley, 1981) and then extended to X-ray data (Toraya, 1986). The method executes the whole pattern decomposition (*i.e.* fitting all the profiles) in one step. In this technique, the peak position $T_j$ in equation (2.3.3.12) is a function of unit-cell parameters, and the unit-cell parameters are refined instead of individual peak positions. Furthermore, the angular dependence of the profile width can be expressed approximately as

$$w(2\theta) = \sqrt{w_1 + w_2 \tan\theta + w_3 \tan^2\theta}, \qquad (2.3.3.20)$$

where $w_1$, $w_2$, and $w_3$ are adjustable parameters (Caglioti, Paoletti & Ricci, 1958); but see also Louër & Langford (1988). The profile-shape dependency on $2\theta$ is ignored when fitting a small $2\theta$ range, but it must be taken into account in the whole-powder-pattern fitting in both focusing and parallel-beam geometries. The least-squares ill conditioning is handled by imposing the constraints on the peak positions in the profile-fitting procedure.

Approximate unit-cell parameters are required to start the refinement. Advantages of this technique are: (1) the unit-cell parameters are refined to high precision; (2) the analysis is rapid and straightforward; (3) it is also powerful in analysing complex powder patterns. The output of indices and integrated intensities of all reflections can be used to calculate Patterson and Fourier diagrams, and thus used for *ab initio* structure determination (McCusker, 1988) and the structure refinement based on the integrated intensities such as used in the *POWLS* program (Will, 1979).

The convolution equation is used in place of $P(x)$ in equation (2.3.3.12), in which the true data function represented by a pseudo-Voigt or Pearson VII has adjustable parameters of crystallite size and strain (Toraya, 1989). The anisotropic crystallite size assuming cylindrical shape has been determined by whole-powder-pattern fitting for complex powder patterns.

The advantage of profile fitting is illustrated in Fig. 2.3.3.10 for the quartz cluster at 68° with Cu $K\alpha$ where the doublet separation is 0.19° and the FWHM is 0.14°. The relative intensities of the 122, 203, and 301 $K\alpha_1$ peaks are 81:97:100, which differ from the profile-fitted peaks, 90:100:67, due to the overlapping. The sum of the fitted curves is the solid line which passes through the experimental points. The peak-search (or strip-chart) intensities that are not corrected for overlaps are more likely to correspond to the ICDD powder file than the profile-fitted values. Profile fitting is capable of about $\pm 0.0004°2\theta$ and 0.2% intensity for good experimental data (Parrish & Huang, 1980). Even in data with poor counting

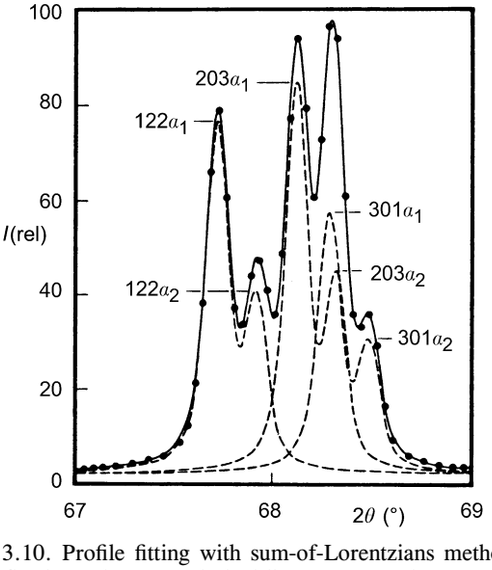


Fig. 2.3.3.10. Profile fitting with sum-of-Lorentzians method. Individual reflections shown as dashed-line curves and sum as solid line passing through experimental points. Quartz peak cluster, Cu $K\alpha_1$, $K\alpha_2$, conventional diffractomer.

statistical accuracy, it is possible to identify very weak peaks with low $P/B$ as shown in Fig. 2.3.3.11.

### 2.3.3.9. *Computer graphics for powder patterns*

An interactive graphics display program is a very important asset for interpreting and analysing powder diffraction data. If a colour graphics station is used, the display can be enhanced by using various colours. The simplest form is the VDU display of experimental points connected with straight lines, which appears similar to a strip-chart recording but has no time-constant error and is printed on page-size paper. It avoids storing large numbers of charts because hundreds of patterns can be stored on a diskette and displayed and printed at any time.

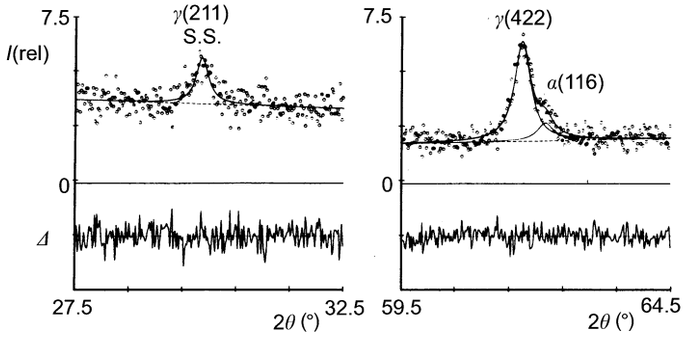


Fig. 2.3.3.11. Profile fitting of poor statistical data.

The basic parameters required in one of the published methods (Parrish, Huang & Ayers, 1984) are the $d$'s and $I$'s of the reflections, the wavelength and profile shapes ($\lambda * G$ instrument function). This makes it possible to produce a pattern exactly as it would appear on the user's diffractometer, aside from contributions arising from sample microstructure. The step size can be included if experimental patterns are to be reproduced or if patterns are to be subtracted. A section of the pattern can be enlarged to the full screen size by entering the desired angular range and highest peak intensity. A linear background can be added by entries at the low- and high-$2\theta$ points. Nonlinear background, *e.g.* from an amorphous substrate, can be transferred from a stored file. Counting statistical noise can be added to a simulated pattern by using a normally distributed random number with a standard deviation scaled to the calculated $I^{1/2}$. Noise in an experimental pattern can be smoothed. A profile broadening factor can be added to the $\lambda * G$ function. Quantitative synthesis of a mixture can be simulated by entering the relative weight percentage and reference intensity, the ratio of the intensities of the strongest lines of each pattern in a 50–50 mixture, or the ICDD values compared to $\alpha$-$Al_2O_3$ (de Wolff & Visser, 1988; Davis & Smith, 1988). The program has access to the ICDD file stored on disk so that any card can be reproduced as a pattern using any wavelength. Some examples are shown in Fig. 2.3.3.12.

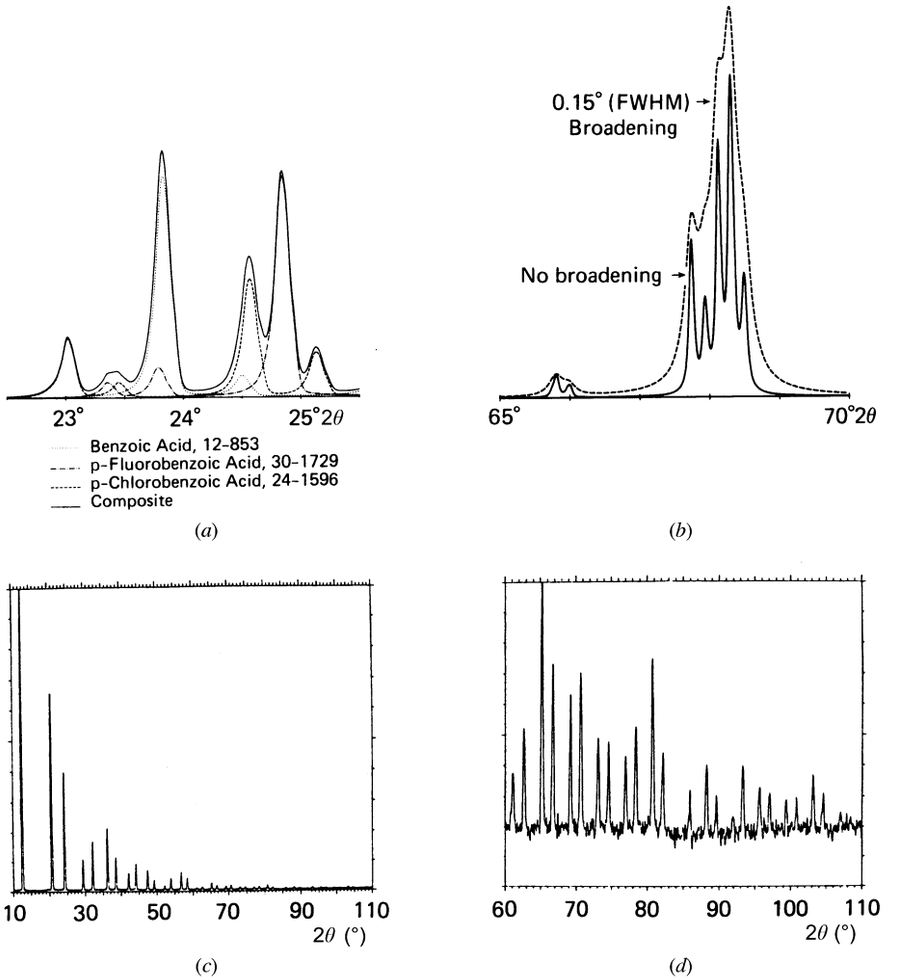


Fig. 2.3.3.12. Some examples of computer graphics of powder patterns. (*a*) Overlay of three patterns with ICDD card numbers. (*b*) Effect of adding 0.15° to FWHM. (*c*) Synchrotron 0.6888 Å radiation pattern of Si powder. (*d*) Low-intensity section enlarged and 11-point smoothing.



references